Electrical Power and Energy Systems 133 (2021) 107263

Contents lists available at ScienceDirect

International Journal of Electrical Power and Energy Systems

journal homepage: www.elsevier.com/locate/ijepes

Dual multivector model predictive control for the power converters of a floating OWC WEC

Marcos Blanco [a], Dionisio Ramirez [b,*], Mohammad Ebrahim Zarei [c], Mahima Gupta [d]

[a] Centro de Investigaciones Energéticas, Medioambientales y Tecnológicas (CIEMAT). Av. Complutense, 40, 28040 Madrid, Spain
[b] Centro de Electrónica Industrial (CEI), Jose Gutierrez Abascal 2, 28002 Madrid, Spain
[c] Electrical Systems Unit, IMDEA Energy, Avda. Ramón de la Sagra 3, 28935 Móstoles, Madrid, Spain
[d] Portland State University, 1930 SW Fourth Avenue, Portland, OR 97201, United States

ARTICLE INFO

Keywords:
Model predictive control
MMPC
MPC
Wave energy
OWC

ABSTRACT

Oscillating Water Column (OWC) is one of the most well-known wave energy converter (WEC). Typically, OWCs are installed in rocky shores or in custom-built breakwaters. However, since the wave profile is more favorable in an open sea, it can also be installed in a point absorber in order to increase the energy extraction.

This paper presents the development of a new dual Multivector Model Predictive Control (MMPC) for the power converters of a floating OWC WEC. The fast dynamic response featured by the proposed MMPC has proven to be very suitable to deal with the highly variable torque and velocity of the turbines present in this type of WECs, achieving an outstanding tracking of the references. Besides, the dual MMPC provides high-quality current to the electric generator and to the grid. The performance of the MMPC for floating OWC WEC has been tested in the laboratory by implementing the mathematical model of the complete OWC WEC installed on a buoy, in the real-time controller of an emulator. The model is based on Thevenin equivalent theorem to simplify the calculation of the force generated by the power take-off (PTO) system.

1. Introduction

The OWC WEC is a type of wave energy converter, which takes advantage of the differential pressure between the air chamber and the external environment created by the ocean waves. This technology of WEC was one of the first concepts to be implemented [1] and nowadays its state of development is relatively advanced compared with other WEC concepts, with TRL values of 8 in OWC based on shoreline fixed air chambers, and TRL values of 7 in OWC integrated into floating offshore WECs [2].

OWC WECs PTO, like in most of the renewable energy generators, comprises of one grid side converter (GSC) and one machine side converter (MSC). The control of both converters is ultimately intended to impose a velocity or torque reference in the electric generator and can be carried out using several different technologies, typically based on space vectors. Field-oriented control (FOC) is one of the most common control approaches and features fixed switching frequency, low power ripple, and uses several PI controllers. However, any perturbation in the system or in the grid reduces the performance of the controller [3,4]. Other systems such as direct torque control (DTC) feature fast and robust dynamic response but largely depend on the sampling frequency of the microcontroller [5].

Some advanced systems designed to control the rotation speed of the electric generator connected to the turbine of OWC WECs have been recently published. In [6], an event-triggered backstepping controller (ET-BSC) and an event-triggered sliding mode controller (ET-SMC) have been successfully tested with the ET-BSC and showcase better performance than the ET-SMC. Other proposals make use of a maximum power point tracking controller [7] to adjust the speed of the DFIG according to an established curve. All these controls are designed to avoid operation at the power output limit which is caused by the stalling of the Wells turbine. Besides, some complementary controls such as controlling the airflow through the throttle valve [8] or smoothing the oscillations of the generated power by means of storage [9,10] have been proposed.

The dual control system presented in this paper features two different MPCs, one for each converter, which are modified to use multiple vectors in each switching cycle, and are therefore named Multivector Model Predictive Control (MMPC). In the 1980s, traditional Model Predictive Control (MPC) was developed to overcome the limitations of traditional methods such as FOC and DTC. In renewable

* Corresponding author.
E-mail address: dionisio.ramirez@upm.es (D. Ramirez).

https://doi.org/10.1016/j.ijepes.2021.107263
Received 23 September 2020; Received in revised form 21 May 2021; Accepted 22 May 2021
Available online 4 June 2021

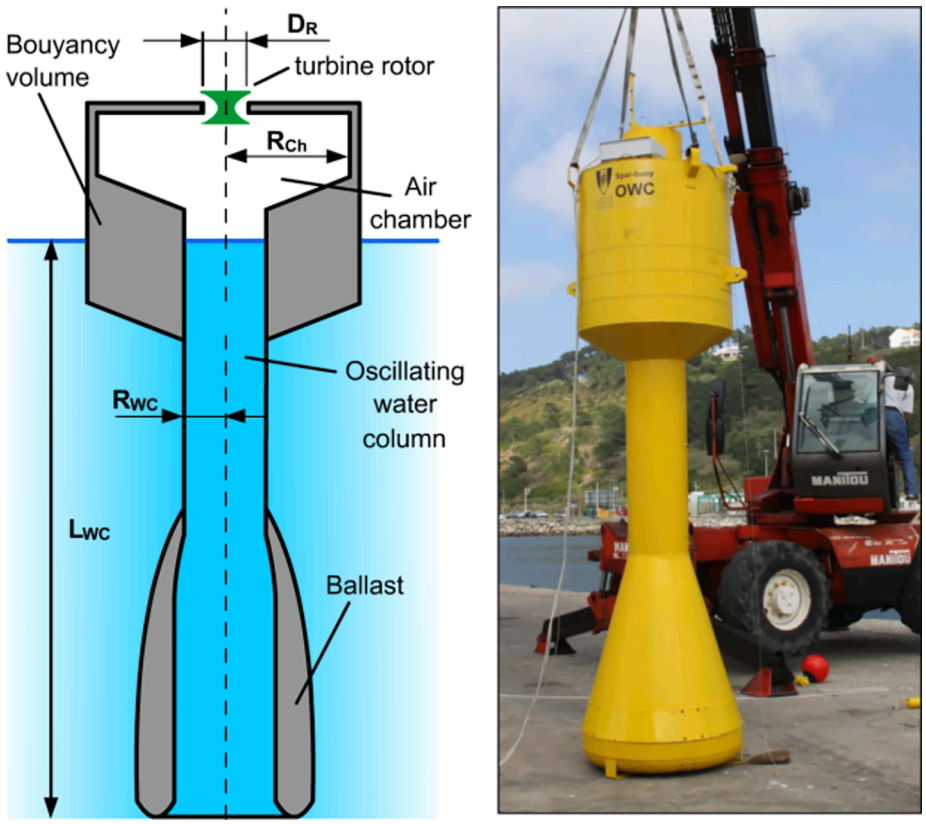

Fig. 1. Scheme (left) and photography (right) of a floating OWC WEC [16].

energy applications, MMPC, like traditional MPC, relies on the electric model of the generator or the grid connection and, therefore, is sensitive to parameter changes. Another trade-off is the computation intensive implementation of a cost function which is used to assess all pairs of adjacent vectors and is, therefore, time-consuming. However, their dynamic response is very fast, and the reference tracking errors are very low. Besides, in traditional MPC, the cost function minimization provides the duration times of the space vectors used in the modulation, which eliminates the need to use a space vector modulator (SVM).

Specifically, in wave energy applications, the fast dynamic response provided by the proposed MMPC of the MSC allows a fast control of the generator, necessary to deal with the highly dynamic conditions of the OWC WEC and the almost ripple-free current generated by the MSC. Further, the GSC reduces losses and provides a high-quality current to the generator and the grid. In addition, the MPC modified to use multiple vectors in each switching cycle (MMPC) presented in this paper overcomes the need for assessing all the pairs of vectors, saving an important amount of computing time.

This paper also presents a new detailed model of an OWC WEC based on a piston approach [11,12,13] and a uniform pressure distribution model [14]. The model evaluates the dynamic of the point absorber and the water column (in particular, its relative velocity), establishing an equivalence electric variables (eg. electric currents and velocities) in an analog Thevenin equivalent circuit. This method reduces the computational burden associated with the mathematical model and allows to run it very fast in a microcontroller (MCU) in the laboratory. The model is used in a laboratory test bench to test the performance of the proposed MMPC.

The paper is organized as follows. Firstly, Section 2 provides a brief description of the OWC WEC used. Then, Section 3 presents the proposed dual MMPC as well as the modulation of the resulting reference voltage vectors, is presented. Next, the OWC WEC emulator model is described in Section 4 which also discusses the results obtained using MATLAB-Simulink and, in the laboratory, using the emulator. Finally, Section 5 summarizes the paper and presents conclusions.

2. OWC WEC system description

The OWC WEC is a type of wave energy converter, which features an internal air chamber and oscillating water column within a rigid exterior hull. When perturbed by sea waves, the relative motion between the free surface of the water column and the rigid hull creates a differential pressure between the air chamber and the external environment. This differential pressure drives an airflow across an air turbine which, in turn, provides mechanical power to a rotating generator. The rigid hull can be fixed to the shoreline or the seabed or, like in the case considered in this paper, it can be floating and restrained by compliant moorings [15].

The OWC WEC used in this paper, Fig. 1, is an axisymmetric device (insensitive to wave direction) consisting basically of a (relatively long) submerged vertical tube that is open at both ends and is fixed to a floater that moves in a heave [16]. It comprises of 2 bodies: the point absorber itself, composed of floater and tail tube (body 1), and the water inside the chamber, modeled as a weightless rigid piston (body 2). The OWC diameter is assumed to be much smaller than the wavelength [17]. The dimensions are listed in Table 2.

There is a Wells turbine at top of the WEC which is driven by the airflow induced by the OWC movement. The turbine shaft is connected to a permanent magnet generator which is controlled by a power electronic converter and a second power electronic converter connects the system to the electric grid.

3. Multivector model predictive control of the power converters

The OWC WEC is controlled by means of a machine side converter (MSC) connected to the electric generator and a grid side converter

(GSC) that delivers the generated energy to the grid. Both converters are controlled using the proposed dual MMPC although they use different references (torque and magnetic field vs. active and reactive powers) and use different reference frames which lead to different mathematical developments and results, as is shown in the following subsections.

3.1. MMPC of the machine side converter

Extracting the maximum power from the waves means that the torque of the electric generator, a permanent magnet generator (PMSG) in this case, must be controlled following a certain strategy that maximizes the power exchange between the Wells turbine and the generator. There are several possible strategies to control an OWC based power generator [18,19]. Nowadays there are advanced WEC controls based on autoregressive methods [20,21], artificial neural networks [22] and fuzzy systems [23] that take into consideration the sea variability. However, a simpler but still adequate control strategy for the purpose of this work (the control of the power converters) is to generate a load torque proportional to the square of the rotor speed [18] since it circumvents the need to periodically evaluate the sea state (to set the numerical values for the parameters appearing in the control equations).

$$T_{PTO} = k_t \cdot \omega_r^2 (\omega_r = N) \tag{1}$$

The MMPC of the MSC uses Eq. (1) as reference to control the PMSG torque through the q component of the stator current, i_{sq}

$$T_e = \frac{3}{2} p \lambda_f i_{sq} \tag{2}$$

Meanwhile, the magnetic field must be maintained to the rated value by keeping $i_{sd} = 0$, except if rotor speed exceeds its rated value.

The MMPC is based on its electric model of the PMSG (see Table 4 for nomenclature). The electric equations expressed in the rotor rotating reference frame, d-q frame, are

$$v_{MSCd} = v_{sd} = R_s i_{sd} + \frac{d}{dt}\lambda_{sd} - \omega_r \lambda_{sq} \tag{3}$$

$$v_{MSCq} = v_{sq} = R_s i_{sq} + \frac{d}{dt}\lambda_{sq} + \omega_r \lambda_{sd} \tag{4}$$

where v_{sd}, v_{sq} represent the stator voltage in d-q axes and the stator flux of SPMSG in the d-q frame is

$$\lambda_{sd} = L_s i_{sd} + \lambda_f \tag{5}$$

$$\lambda_{sq} = L_s i_{sq} \tag{6}$$

The load torque produced by the PMSG, opposite to the turbine torque, can be calculated by using the equation

$$T_e = \frac{3}{2} p \left(\lambda_{sd} i_{sq} - \lambda_{sq} i_{sd} \right) \tag{7}$$

Eq. (5), Eq. (6), and Eq. (7) express that it is possible to control the PMSG torque and magnetic field by means of i_{sq} and i_{sd}. In the last stage of the control system, the space vector modulator (SVM) applies three space vectors, $\vec{v}_a$, $\vec{v}_b$, $\vec{v}_c$, one by one in a symmetrical way, in every program cycle, giving rise to changes in the stator current.

In d-q coordinates, according to Eqs. (3) and (4), the derivative of the stator current (or current slopes generated by each space vector) for each of the selected space vectors can be calculated as

$$\frac{d}{dt} i_{sd} = S_{id} = \frac{1}{L_s} \left(-R_s i_{sd} + \omega_r L_s i_{sq} + v_{sd} \right) \tag{8}$$

$$\frac{d}{dt} i_{sq} = S_{iq} = \frac{1}{L_s} \left(-R_s i_{sq} - \omega_r L_s i_{sd} - \omega_r \lambda_f + v_{sq} \right) \tag{9}$$

In the MMPC presented in this paper, the prediction horizon is assumed to be 1. Different objectives can be considered to control the electrical machine. In this paper, the objective is to reduce the stator current error in the synchronous frame for the upcoming switching period, instant k + 1. Hence, the following quadratic cost function is considered to reduce the stator current at instant k + 1

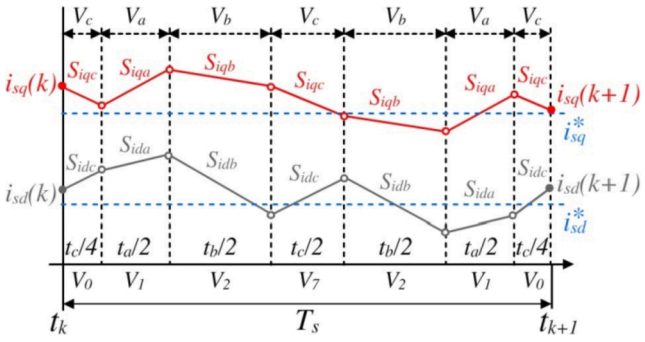

Fig. 2. Current variations in the synchronous frame in the kth switching period caused by the application of $\vec{v}_a$, $\vec{v}_b$, $\vec{v}_c$.

$$F(k+1) = \left(i_{sd}(k+1) - i_{sd}^*(k+1) \right)^2 + \left(i_{sq}(k+1) - i_{sq}^*(k+1) \right)^2 \tag{10}$$

where, the superscript * denotes the reference values.

Since the switching intervals are small, it is assumed that the stator current at instant k + 1 is the same as instant k, which means that

$$i_{sd}^*(k+1) = i_{sd}^*(k)$$

$$i_{sdq}^*(k+1) = i_{sq}^*(k) \tag{11}$$

In the proposed MMPC method, three voltage vectors, $\vec{v}_a$, $\vec{v}_b$ and $\vec{v}_c$, are applied in each switching interval symmetrically, as shown in Fig. 2. According to Fig. 2, the stator current at instant k + 1 can be predicted from the stator current value at instant k and the current slopes of the vectors and their duration times in this period. According to Fig. 2, the stator current at the instant k + 1 can be represented by

$$i_{sd}(k+1) = i_{sd}(k) + S_{ida} t_a + S_{idb} t_b + S_{idc} t_c \tag{12}$$

$$i_{sq}(k+1) = i_{sq}(k) + S_{iqa} t_a + S_{iqb} t_b + S_{iqc} t_c \tag{13}$$

where S_{idj} and S_{iqj}, are the current slopes (d and q axes respectively) generated by the successive application of the vectors, $\vec{v}_a$, $\vec{v}_b$, $\vec{v}_c$, calculated using Eq. (8) and Eq. (9). As a result, according to Eqs. (10)-(13), the proposed cost function at instant k + 1 can be represented as

$$F(k+1) = \left(i_{sd}(k) + S_{ida} t_a + S_{idb} t_b + S_{idc} t_c - i_{sd}^*(k) \right)^2 + \left(i_{sq}(k) + S_{iqa} t_a + S_{iqb} t_b + S_{iqc} t_c - i_{sq}^*(k) \right)^2 \tag{14}$$

The optimal duration time of vectors should be predicted in order to minimize the proposed cost function in each period. Hence, the derivatives of the cost function with respect to the t_a and t_b are estimated and are set to zero. This means that

$$\frac{\partial F(k+1)}{\partial t_a} = 0 \tag{15}$$

$$\frac{\partial F(k+1)}{\partial t_b} = 0 \tag{16}$$

By solving the above equations, the optimal duration times of vectors result in

$$t_a = \frac{\left(i_{sd}(k) - i_{sd}^*(k)\right)\cdot\left(S_{iqb} - S_{iqc}\right) + \left(i_{sq}(k) - i_{sq}^*(k)\right)\cdot\left(S_{idc} - S_{idb}\right)}{S_{iqa}(S_{idb} - S_{idc}) + S_{iqb}(S_{idc} - S_{ida}) + S_{iqc}(S_{ida} - S_{idb})} + \frac{T_s\left(S_{iqb}\cdot S_{idc} - S_{iqc}\cdot S_{idb}\right)}{S_{iqa}(S_{idb} - S_{idc}) + S_{iqb}(S_{idc} - S_{ida}) + S_{iqc}(S_{ida} - S_{idb})} \quad (17)$$

$$t_b = \frac{\left(i_{sd}(k) - i_{sd}^*(k)\right)\cdot\left(S_{iqc} - S_{iqa}\right) + \left(i_{sq}(k) - i_{sq}^*(k)\right)\cdot\left(S_{ida} - S_{idc}\right)}{S_{iqa}(S_{idb} - S_{idc}) + S_{iqb}(S_{idc} - S_{ida}) + S_{iqc}(S_{ida} - S_{idb})} + \frac{T_s\left(S_{iqc}\cdot S_{ida} - S_{iqa}\cdot S_{idc}\right)}{S_{iqa}(S_{idb} - S_{idc}) + S_{iqb}(S_{idc} - S_{ida}) + S_{iqc}(S_{ida} - S_{idb})} \quad (18)$$

$$t_c = T_s - t_a - t_b \quad (19)$$

When the optimal duration times of vectors are estimated, the equivalent voltage vector that should be applied to minimize the cost function , $\vec{v}_{ref}$, in the stationary reference frame can be estimated by

$$\vec{v}_{refMSC} = v_{ref\alpha} + jv_{ref\beta} = \vec{v}_a\cdot\frac{t_a}{T_s} + \vec{v}_b\cdot\frac{t_b}{T_s} + \vec{v}_c\cdot\frac{t_c}{T_s} \quad (20)$$

3.2. MMPC of the grid side converter

The GSC is in charge of sending the incoming power from the PMSG to the grid in order to keep the DC link voltage constant. The reactive power reference is kept to zero, although under some grid disturbances it could be necessary to deliver reactive power to fulfill the grid code, common for wind generators.

The MMPC is developed from the electric equations of the grid connection. The most advantageous reference frame is the stationary frame (α,β) since it avoids the need to carry out the Park transformation, which saves computation time and makes it unnecessary to use a PLL for grid synchronization.

The relationship between the GSC voltage and the grid voltage is (see Table 5 for nomenclature)

$$\vec{v}_{GSC} = \vec{v}_g + L_f\frac{d\vec{i}_g}{dt} + R_f\vec{i}_g \quad (21)$$

The active and reactive powers delivered by the GSC to the grid can be calculated as

$$P_g = 1.5\cdot\left(v_{g\alpha}i_{g\alpha} + v_{g\beta}i_{g\beta}\right) \quad (22)$$

$$Q_g = 1.5\cdot\left(v_{g\beta}i_{g\alpha} - v_{g\alpha}i_{g\beta}\right) \quad (23)$$

and the derivatives of these powers are

$$\frac{dP_g}{dt} = 1.5\left(\frac{dv_{g\alpha}}{dt}i_{g\alpha} + \frac{di_{g\alpha}}{dt}v_{g\alpha} + \frac{dv_{g\beta}}{dt}i_{g\beta} + \frac{di_{g\beta}}{dt}v_{g\beta}\right) \quad (24)$$

$$\frac{dQ_g}{dt} = 1.5\left(\frac{dv_{g\beta}}{dt}i_{g\alpha} + \frac{di_{g\alpha}}{dt}v_{g\beta} - \frac{dv_{g\alpha}}{dt}i_{g\beta} - \frac{di_{g\beta}}{dt}v_{g\alpha}\right) \quad (25)$$

The grid voltage can be represented by means of the $\alpha-\beta$ components of its space vector

$$v_{g\alpha} = v_g cos\omega_s t \quad (26)$$

$$v_{g\beta} = v_g sin\omega_s t \quad (27)$$

and the derivatives of this voltage in the stationary frame are

$$\frac{dv_{g\alpha}}{dt} = -\omega_s v_g sin\omega_s t = -\omega_s v_{g\beta} \quad (28)$$

$$\frac{dv_{g\beta}}{dt} = \omega_s v_g cos\omega_s t = \omega_s v_{g\alpha} \quad (29)$$

According to Eq. (21), the derivative of the grid current can be calculated as

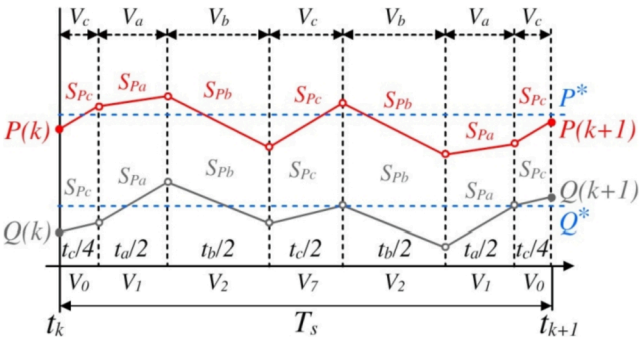

Fig. 3. Active and reactive power variations in the kth switching period caused by the application of $\vec{v}_a$, $\vec{v}_b$, $\vec{v}_c$.

$$\frac{di_{g\alpha}}{dt} = \frac{v_{GSC\alpha} - v_{g\alpha} - R_f i_{g\alpha}}{L_f} \quad (30)$$

$$\frac{di_{g\beta}}{dt} = \frac{v_{GSC\beta} - v_{g\beta} - R_f i_{g\beta}}{L_f} \quad (31)$$

Now, by substituting Eqs. (28)–(31) into Eq. (24) and Eq. (25), it is possible to obtain the corresponding power variations that each of the GSC voltage vectors causes in the grid connection

$$\frac{dP_g}{dt} = S_P = \frac{1.5}{L_f}\left[\left(v_{g\alpha}v_{GSC\alpha} + v_{g\beta}v_{GSC\beta}\right) - \left(v_{g\alpha}^2 + v_{g\beta}^2\right)\right] - \frac{R_f}{L_f}P_g - \omega_s Q_g \quad (32)$$

$$\frac{dQ_g}{dt} = S_Q = \frac{1.5}{L_f}\left[\left(v_{g\beta}v_{GSC\alpha} - v_{g\alpha}v_{GSC\beta}\right)\right] - \frac{R_f}{L_f}Q_g + \omega_s P_g \quad (33)$$

The prediction horizon for the MPPC of GSC is also considered to be 1. The objective of the GSC is to decrease the GSC active and reactive power errors for the upcoming switching period, instant k + 1. In this case, the active and reactive powers reach the references as much as it is possible by the cost function. As a result, the following cost function is considered to reduce the GSC active and reactive power errors at instant k + 1

$$G(k+1) = \left(Q_g(k+1) - Q_g^*(k+1)\right)^2 + \left(P_g(k+1) - P_g^*(k+1)\right)^2 \quad (34)$$

where, the superscript * denotes the reference values.

Since the periods are small, it is considered that the GSC active and reactive powers at instant k + 1 is the same as instant k, which means that

$$P_g^*(k+1) = P_g^*(k)$$

$$Q_g^*(k+1) = Q_g^*(k) \quad (35)$$

In the proposed MMPPC for the GSC, three voltage vectors are applied in each period like for the machine side converter. By adding the effect of all the GSC voltage vectors successively to the power value at the beginning of the cycle (instant k), it is possible to obtain the future power value at the end of the coming switching cycle (instant k + 1)

$$P_g(k+1) = P_g(k) + S_{Pa}t_a + S_{Pb}t_b + S_{Pc}t_c \quad (36)$$

$$Q_g(k+1) = Q_g(k) + S_{Qa}t_a + S_{Qb}t_b + S_{Qc}t_c \quad (37)$$

where, S_{Pi} and S_{Qi} are the power variations for each voltage vector $\vec{v}_a$, $\vec{v}_b$, and $\vec{v}_c$, calculated using Eq. (32) and Eq. (33). The application pattern of the three voltage vectors in a period for the GSC and their effects on active and reactive power are shown in Fig. 3. Consequently, according to Eqs. (34)-(37), the cost function can be expressed by

$$G(k+1) = \left(Q_g(k) + S_{Qa}t_a + S_{Qb}t_b + S_{Qc}t_c - Q_g^*(k)\right)^2 + \left(P_g(k) + S_{Pa}t_a + S_{Pb}t_b + S_{Pc}t_c - P_g^*(k)\right)^2 \quad (38)$$

In order to minimize the proposed cost function for the GSC, the optimal duration times of vectors in each interval should be estimated. Consequently, the derivatives of the proposed cost function for the GSC with respect to the t_a and t_b are set to zero to obtain the optimal duration times. This means that

$$\frac{\partial G(k+1)}{\partial t_a} = 0 \quad (39)$$

$$\frac{\partial G(k+1)}{\partial t_b} = 0 \quad (40)$$

According to the Eqs. (39) and (40), the corresponding optimal duration times of each vector result in

$$t_a = \frac{\left(P_g(k) - P_g^*(k)\right)\cdot(S_{Qb} - S_{Qc}) + \left(Q_g(k) - Q_g^*(k)\right)\cdot(S_{Pc} - S_{Pb})}{S_{Qc}(S_{Pa} - S_{Pb}) + S_{Qa}(S_{Pb} - S_{Pc}) + S_{Qb}(S_{Pc} - S_{Pa})} + \frac{T_s(S_{Qb}\cdot S_{Pc} - S_{Qc}\cdot S_{Pb})}{S_{Qc}(S_{Pa} - S_{Pb}) + S_{Qa}(S_{Pb} - S_{Pc}) + S_{Qb}(S_{Pc} - S_{Pa})} \quad (41)$$

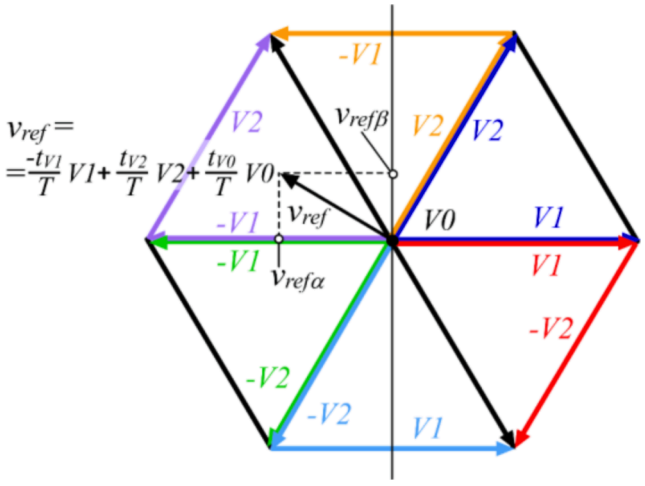

Fig. 4. $\vec{v}_{ref}$ expressed as a combination of $\vec{V}1$, $\vec{V}2$ and $\vec{V}0$.

$$t_b = \frac{\left(P_g(k) - P_g^*(k)\right)\cdot(S_{Qc} - S_{Qa}) + \left(Q_g(k) - Q_g^*(k)\right)\cdot(S_{Pa} - S_{Pc})}{S_{Qc}(S_{Pa} - S_{Pb}) + S_{Qa}(S_{Pb} - S_{Pc}) + S_{Qb}(S_{Pc} - S_{Pa})} + \frac{T_s(S_{Qc}\cdot S_{Pa} - S_{Qa}\cdot S_{Pc})}{S_{Qc}(S_{Pa} - S_{Pb}) + S_{Qa}(S_{Pb} - S_{Pc}) + S_{Qb}(S_{Pc} - S_{Pa})} \quad (42)$$

$$t_c = T_s - t_a - t_b \quad (43)$$

The GSC average voltage vector, $\vec{v}_{refGSC}$, that should be applied to minimize the cost function in the stationary reference frame can be estimated by

$$v_{refGSC} = v_{ref\alpha} + jv_{ref\beta} = \vec{v}_a\cdot\frac{t_a}{T_s} + \vec{v}_b\cdot\frac{t_b}{T_s} + \vec{v}_c\cdot\frac{t_c}{T_s} \quad (44)$$

3.3. Multivector modulation

The next step in both MMPCs (MSC and GSC) is to reproduce $\vec{v}_{ref}$ using modulation. When $\vec{v}_{ref}$ is located in the first sector, the vectors $\vec{v}_a$, $\vec{v}_b$, and $\vec{v}_c$ used in the modulation stage shall be $\vec{V}1$, $\vec{V}2$ and $\vec{V}0$, Fig. 4, but they must change as $\vec{v}_{ref}$ rotates throughout the six sectors. In effect, the vectors $\vec{v}_a$, $\vec{v}_b$, $\vec{v}_c$ must be those that minimize the corresponding cost function and have positive duration times. There are two methods to choose them [24,25,26]: a) searching the sector where $\vec{v}_{ref}$ is located and selecting the adjacent vectors that define that sector, b) assessing the effect of the six pairs of adjacent vectors and choose the one that minimizes the cost function. In both cases, the task is time consuming. From the point of view of $\vec{v}_{ref}$ calculation, it is preferable to suppose that $\vec{v}_a$, $\vec{v}_b$, $\vec{v}_c$ are always $\vec{V}1$, $\vec{V}2$ and $\vec{V}0$ [27]. Note, Fig. 4, that any $\vec{v}_{ref}$ can be expressed by the linear combination of $\vec{V}1$, $\vec{V}2$ and $\vec{V}0$ in the six sectors. In this case, the duration times calculations for $\vec{V}1$, $\vec{V}2$ could have negative values which indicates that the voltage vector should have negative value, as presented in Fig. 4. As a result, according to Eqs. (20) and (44) and considering that the vectors $\vec{v}_a$, $\vec{v}_b$, $\vec{v}_c$ are $\vec{V}1$, $\vec{V}2$ and $\vec{V}0$, respectively, and t_a, t_b, t_c their estimated duration times, the $\vec{v}_{ref}$ is obtained. It should be noted that, if the duration time of the zero vector obtains a negative value, this means that the modulation index will be greater than 1 and therefore the equivalent voltage must be limited to the maximum modulation index value which is 1.

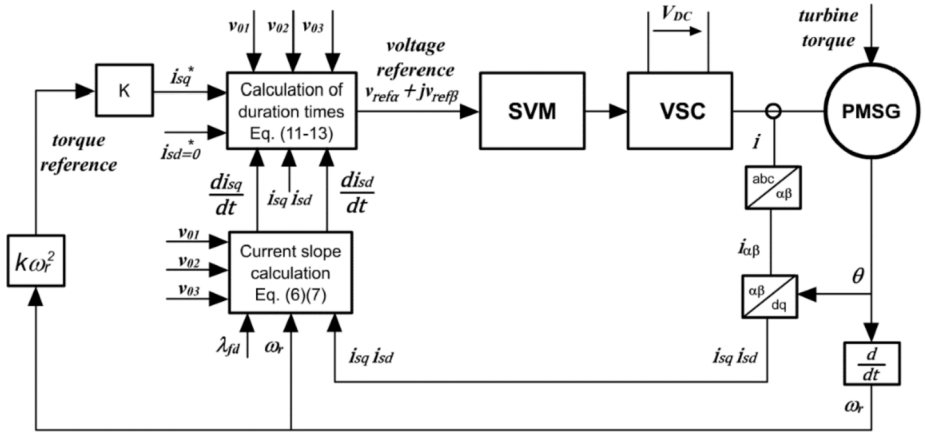

Fig. 5. Block diagram of the MMPC for the MSC.

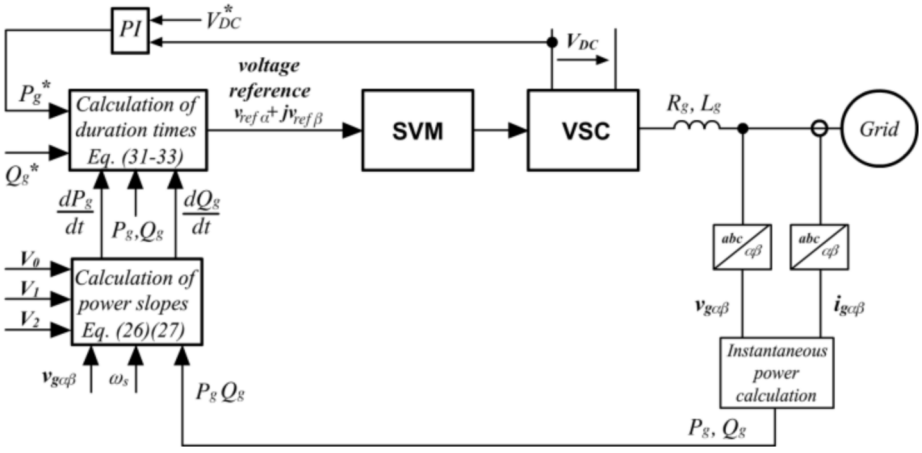

Fig. 6. Block diagram of the MMPC for the GSC.

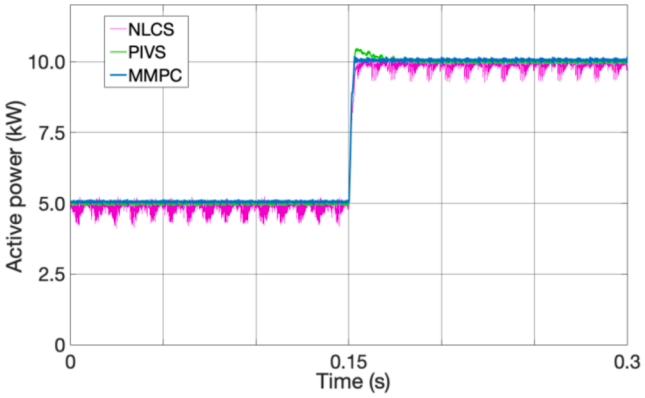

Fig. 7. Step response of several control techniques for comparison.

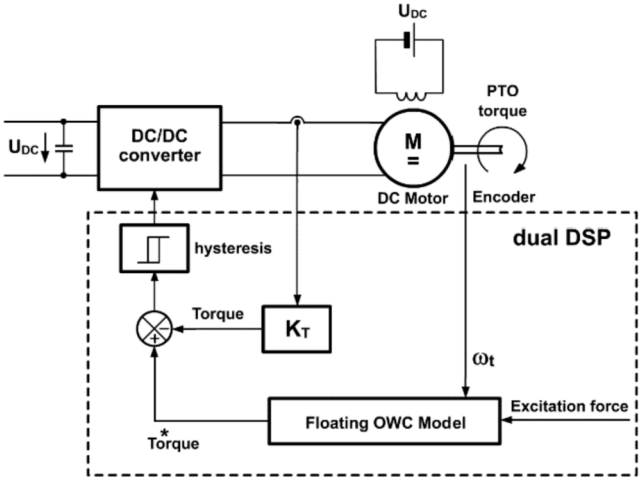

Fig. 8. OWC WEC emulator.

Then, once $\vec{v}_{ref}$ has been calculated, its components $(v_{ref\alpha}, v_{ref\beta})$ are sent to a Space Vector Modulator (SVM) that readily finds the location of $\vec{v}_{\text{ref}}$, without using the cost function, and carries out the modulation of v_{ref} using the correct pair of vectors, from $\vec{V}1$ to $\vec{V}6$, plus the zero vector, $\vec{V}0$.

Using this method, the computing time for the MMPC keeps low and the switching frequency constant.

4. Block diagram

Fig. 5 and Fig. 6 show the block diagrams of the MMPCs which control the torque and magnetic field of the PMSG through the MSC and the MMPC, respectively and control the active and reactive powers delivered by the WEC to the grid.

5. Comparison with other control techniques

The proposed MMPC of the GSC has been tested in simulation against a classic voltage source based PI controllers and vector control (PIVS) and a non-linear current source (NLCS) [28] for the same parameters such as switching frequency, filter, etc., Fig. 7. The results show that whereas PIVS demonstrates the fastest dynamic response, it presents a slight overshoot (which depends on the values of PI constants). The NLCS features a high ripple magnitude. On the other hand, the MMPC approach provides a critically damped and cleaner response.

6. Laboratory test rig – Emulation of the OWC WEC system

The PMSG and grid connection MMPCs have been tested in the laboratory, in a custom-built emulator which includes a model of the floating OWC WEC system, Fig. 8, Fig. 9, and Fig. 10.

A separately excited 7.8 kW DC motor, see Table 6, and a DC/DC converter featuring hysteresis band control is used to control the armature current which tracks the torque reference of the emulated turbine. This DC motor and DC/DC converter is used to emulate the complete OWC WEC system.

An 8.7 kW PMSG, see Table 7, is used as electric generator and a three phase voltage source converter (VSC) featuring MMPC generates the load torque that extracts the energy from the PTO and sends it to the DC link. Finally, a third converter, featuring MMPC, sends the generated power to the grid, keeping the DC link voltage constant. The whole emulator is controlled by six MCUs (three F28335 and three ARM Cortex M3 grouped into three dual-core F28M35x Concerto) by Texas Instruments. The code of the six microcontrollers was programmed in C-language and the computing time resulted around 50 μs for the MMPC and 21 μs for the SVM.

If it is needed to implement an outer control (forecasting, neural, etc.) for the WEC, it is possible to do so by just adding an additional microcontroller devoted to that task and communicated with the rest of microcontrollers that control the power converters using the common Ethernet network.

6.1. *Mathematical model of the OWC WEC system*

As described in Section 2, the WEC considered in this paper is a point

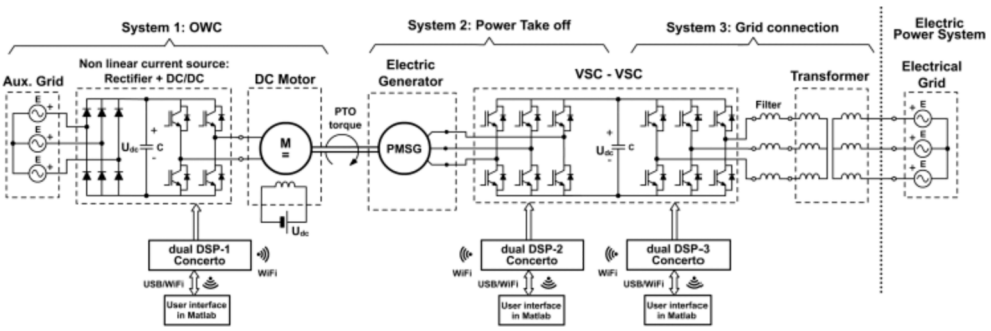

Fig. 9. Electrical scheme of the emulator implemented in the lab.

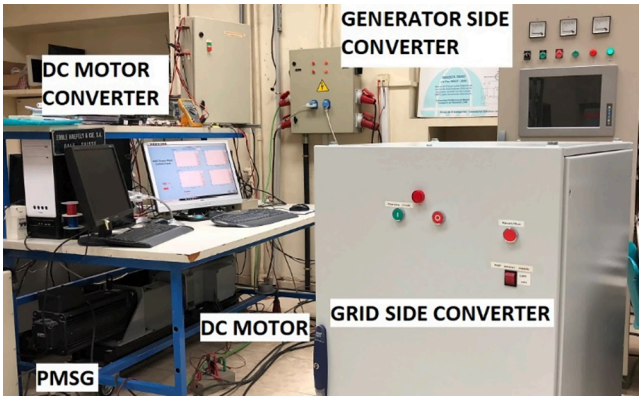

Fig. 10. Photography of the emulator.

absorber OWC which comprises of 2 bodies: the point absorber itself (body 1) and the water inside the chamber, modeled as a weightless rigid piston (body 2) [29]. The nomenclature used in the development of the model is shown in Table 2 (the OWC dimensions are listed in Table 3). The model obtained is programmed in one of the MCUs of the OWC WEC emulator in the laboratory to carry out the experimental tests.

6.1.1. Point absorber dynamic equations

The model of the OWC point absorber is obtained by the summation of all the forces acting on each body (based on second Newton's law). Two bodies are considered, being body 1 the floating-point absorber and body 2 the free water surface of the water column modelled as a rigid piston. Also, the analysis considers only the heave motion of the bodies, being x_1 and x_2 the heave displacement value of each body and considering its zero-value at the equilibrium point and increasing upwards. In effect, although all equations can be extended to any of the other five degrees of possible motions on the surface of the water, heave motion is the most significant for energy extraction.

The dynamic equations of the two bodies are the result of the summation of all the forces applied to each body [16,30,31]. These dynamic equations can be expressed in terms of velocity, in the Laplace domain, obtaining the following equations

$$\left(m_1 + M_{11}^{\infty}\right)\cdot s\cdot u_1(s) + \varrho_w\cdot g\cdot S_1\cdot\frac{u_1(s)}{s} + M_{12}^{\infty}\cdot s\cdot u_2(s) - p_{at}\cdot S_2\cdot p^* = F_{e,1} - R_{11}{}^*u_1 - R_{12}{}^*u_2 \tag{45}$$

$$\left(m_2 + M_{22}^{\infty}\right)\cdot s\cdot u_2(s) + \varrho_w\cdot g\cdot S_2\cdot\frac{u_2(s)}{s} + M_{21}^{\infty}\cdot s\cdot u_1(s) + p_{at}\cdot S_2\cdot p^* = F_{e,2} - R_{22}{}^*u_2 - R_{21}{}^*u_1 \tag{46}$$

In all cases, the hydrodynamic coefficients (excitation coefficient, radiation impedances, added masses, etc.) have been calculated by analyzing the geometry of the point absorber in the water using the boundary element method (BEM) software WAMIT.

Table 1
Equivalence between mechanical and electrical variables.

Magnitude	
Force	Voltage
Velocity	Current
Displacement	Charge
Impedance	
Mass	Inductance
Damping	Resistance
Spring constant	Inverse of capacitance

The excitation forces are evaluated as the superposition of a certain number of frequency components [16,30], and each components is evaluated as the multiplication of the excitation coefficient by the amplitude of the water free-surface oscillation A_n - for sake of example, the excitation component 'n' of the $F_{e.1}$ is equal to $A_n\cdot f_{e,1}(\omega_n)\cdot cos\left(\omega_n\cdot t + \alpha_{fe,1} + \alpha_n\right)$, where A_n are evaluated considering a Pierson-Moskowitz wave energy spectrum [32].

6.1.2. Air chamber and turbine dynamic equations

The pressure in the air chamber (p^*) is the only variable that can be controlled indirectly by means of the Wells turbine rotation speed. The relationship between the pressure in the chamber and the turbine variables is described below.

If the air inside the chamber is considered as an isentropic fluid during the expansion and compression processes, the relation between air density and air pressure is given by the following linearized equation

$$\dot{\rho} = \frac{\rho_0}{\gamma\cdot p_0}\cdot\dot{p} \tag{47}$$

Defining the volume of air inside the chamber as $V = V_0 + (x_1 - x_2)\cdot S_2$, and the relative velocity between the point absorber and the water column as $u_r = \frac{d}{dt}(x_1 - x_2) = u_1(t) - u_2(t)$; the air mass flow can be calculated as

$$\dot{m} = -\frac{\rho_0\cdot V_0}{\gamma\cdot p_0}\cdot\dot{p} - \rho_0\cdot S_2\cdot u_r \tag{48}$$

Defining the dimensionless parameters, dimensionless pressure as $\Psi = \frac{p}{\rho_0\cdot N^2\cdot D^2}$, and dimensionless flow as $\Phi = \frac{\dot{m}}{\rho_0\cdot N\cdot D^3}$, it is possible to establish a linear relationship, k_t^* [33,34] between dimensionless pressure and dimensionless flow in the Wells turbine

$$k_t^* = \frac{\Psi}{\Phi} = \frac{D\cdot p}{\dot{m}\cdot N} \tag{49}$$

Finally, by substituting Eq. (49) in Eq. (50), the air pressure expressed in the Laplace domain can be written as

$$p(s) = \frac{\varepsilon\cdot u_r(s)}{1 + \varepsilon\cdot\Gamma\cdot s};\ \varepsilon = \frac{L_0}{\gamma\cdot p_0};\ \Gamma = \frac{\rho_0\cdot S_2\cdot N\cdot k_t^*}{D} \tag{50}$$

Table 2
OWC WEC model.

Buoyancy force	
ϱ_w	Sea water density
g	Gravity acceleration
V	Volume of the displaced fluid
$x_1(t)$	Position of the point absorber
$x_2(t)$	Position of the water column
S_1	Point absorber cross section
S_2	Chamber cross section
Hydrodynamic force	
$F_{e,1}(t)$	Excitation force on the point absorber
$F_{e,2}(t)$	Excitation force on the water column
Radiation force	
M_{11}^{∞}	Added mass at infinite frequency to the point absorber
$R_{r11}(t)$	Radiation resistance (damping) of the point absorber
M_{12}^{∞}	Added mass at mutual infinite frequency between point absorber and water column
$R_{r12}(t)$	Mutual radiation resistance (damping) between point absorber and water column
$\dot{x}_1(t)$	Velocity of the point absorber
$\dot{x}_2(t)$	Velocity of the water column
$\ddot{x}_1(t)$	Linear acceleration of the point absorber
$\ddot{x}_2(t)$	Linear acceleration of the water column
M_{22}^{∞}	Added mass at infinite frequency to the water column
$R_{r22}(t)$	Radiation resistance of the water column
Power Take Off	
F_{PTO}	Force generated by the PTO
p_{at}	Atmospheric pressure
p^*	Dimensionless pressure
p	Absolute pressure in the air chamber
u_1	Velocity of the point absorber
u_2	Velocity of the water column
Air chamber	
p_0	Air pressure reference value
ρ_0	Air density reference value
p	Air pressure value
ρ	Air density value
Ψ	Dimensionless pressure
Φ	Dimensionless flow
γ	Isentropic exponent
N	Rotation speed
D	Diameter of the rotor
L_0	Air chamber height, $V_0 = L_0 \cdot S_2$

Table 3
OWC WEC dimensions.

Radius of the water column	$R_{WC} = 2.6$ m
Distance between the water surface and the turbine	$L_0 = 1.0$ m
Turbine rotor diameter	$D_R = 2.1$ m

Table 4
MMPC of PMSG.

$\vec{v}_{MSC}$	Machine side converter voltage vector
$\vec{v}_s$	Stator voltage vector
$\vec{i}_s$	Stator current vector
$\vec{\lambda}_s$	Stator flux vector
ω_r	Electrical rotor speed
R_s	Stator resistance
λ_f	Permanent magnet flux
L_s	Stator inductance
T_e	Electromagnetic torque
p	Number of pole pairs
i	Index of each space vector
S_i	Current slope
S_{da}, S_{db}, S_{dc}	Current slopes in the d axis
S_{qa}, S_{qb}, S_{qc}	Current slopes in the q axis
t_a, t_b, t_c	Duration times
T_s	Switching period

Table 5
MMPC of GSC.

$\vec{v}_{GSC}$	Grid side converter voltage vector
$\vec{v}_g$	Grid voltage vector
$\vec{i}_g$	Grid phase current vector
L_f	Filter inductance
R_f	Filter resistance
P_g	Active power
Q_g	Reactive power
ω_s	Grid angular speed
S_{Pa}, S_{Pb}, S_{Pc}	Active power slopes
S_{Qa}, S_{Qb} S_{Qc}	Reactive power slopes
t_a, t_b, t_c	Duration times.
T_s	Switching period.

Table 6
DC motor rated values.

Rated power	7.8 kW
Rated voltage	400 V
Rated speed	1,092 rpm
K_T	3.5

Table 7
PMSG rated values.

Rated power	8.7 kW
Rated voltage	400 V
Number of pole pairs	3
Permanent magnet Flux	1.05 Wb
Stator Inductance	50 mH
Stator resistance	2 Ω

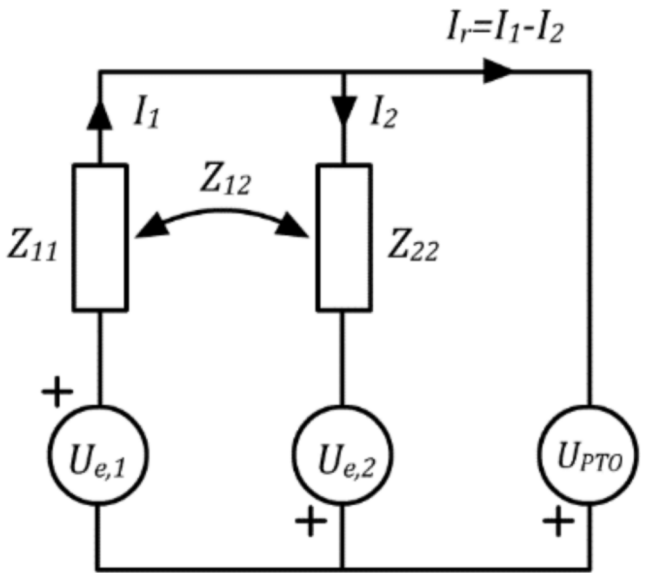

Fig. 11. Equivalent electric circuit to analyze the interaction of forces and the relative motion between the point absorber and the water column.

where the force imposed by the PTO can be expressed in terms of the pressure in the air chamber.

$$\widehat{F}_{PTO} = S_2 \cdot p \tag{51}$$

6.1.3. OWC WEC analog electric circuit

In order to simplify the calculation of u_r, this paper proposes the translation of Eq. (45) and Eq. (46) into an equivalent electrical system. By applying the equivalences shown in Table 1, the following electrical expression are obtained

$$\begin{bmatrix} Z_{11} & Z_{12} \\ Z_{12} & Z_{22} \end{bmatrix} \cdot \begin{bmatrix} I_1 \\ I_2 \end{bmatrix} = \begin{bmatrix} U_1 \\ U_2 \end{bmatrix} \tag{52}$$

where

$$Z_{11} = R_{11} + j \cdot \left[\omega \cdot \left(L_1 + L_{11}^{\infty} \right) - \frac{1}{\omega \cdot C_1} \right] \tag{53}$$

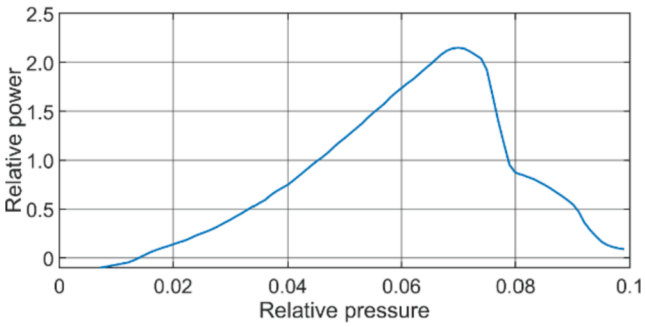

Fig. 13. Dimensionless power, Π, of the Wells turbine vs. dimensionless pressure, Ψ, of the air across the turbine [19].

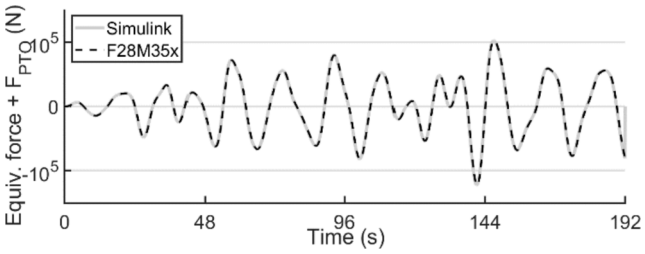

Fig. 14. Summation of the equivalent excitation force and $\widehat{F}_{PTO}$.

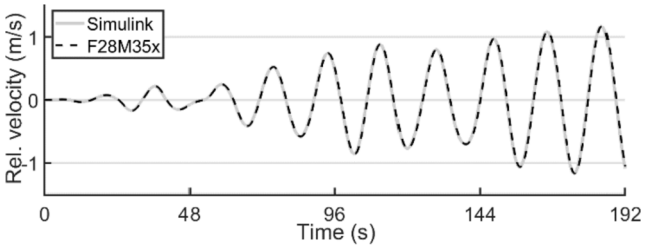

Fig. 15. Relative velocity, u_r.

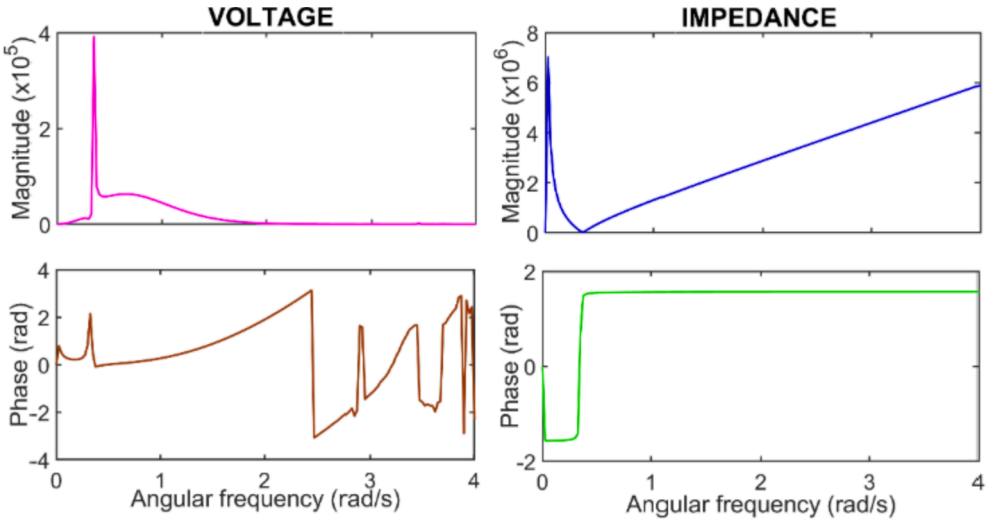

Fig. 12. Magnitude and phase of the Thevenin voltage, U_{Thv}, and impedance, Z_{Thv}, as a function of the angular frequency.

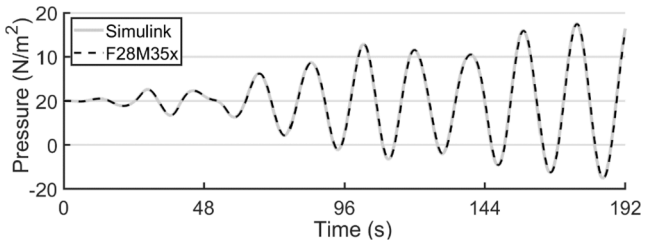

Fig. 16. Pressure in the chamber, p.

$$Z_{22} = R_{22} + j\cdot\left[\omega\cdot\left(L_2 + L_{22}^{\infty}\right) - \frac{1}{\omega\cdot C_2}\right] \tag{54}$$

$$Z_{12} = R_{12} + j\cdot(\omega\cdot L_{12}) \tag{55}$$

This matrix equation can be represented as the electrical circuit of Fig. 11 where, for example, F_{PTO} is represented by U_{PTO}.

Thus, it is possible to obtain a Thevenin equivalent circuit where the system is reduced to a one body equation.

$$Z_{Thv} = \frac{Z_{11}\cdot Z_{22} - Z_{12}^{\,2}}{Z_{11} + Z_{22} + 2\cdot Z_{12}} \tag{56}$$

$$U_{Thv} = \frac{(Z_{22} + Z_{12})\cdot U_{e,1} - (Z_{11} + Z_{12})\cdot U_{e,2}}{Z_{11} + Z_{22} + 2\cdot Z_{12}} \tag{57}$$

Now, obtaining $I_r = I_1 - I_2$ (i.e. u_r)using the equivalent circuit and the forces as voltage sources is immediate: $I_r = (U_{Thv} - U_{PTO})/Z_{Thv}$.

From the values of the coefficients evaluated with WAMIT, U_{Thv} and Z_{Thv} can be calculated as a function of the angular frequency. The magnitude and phase of these two variables are shown in Fig. 12.

The frequency response of the floating OWC WEC, Fig. 12, can be realized as state space or as a transfer function in the Laplace domain, as it is explained in [35,36]. This transfer function representation, along with the air chamber transfer function, Eq. (50), and Eq. (51), allow simulating the dynamic system response of the OWC WEC.

Finally, the power extracted by the OWC is evaluated form the dimensionless power of the Wells turbine, defined as $\Pi = \frac{P}{\rho_0\cdot N^3\cdot D^5} = \frac{(T_{PTO}\cdot N)}{\rho_0\cdot N^3\cdot D^5}$. The relation between its dimensionless power, Π, and the dimensionless pressure, Ψ, depends on the configuration of the turbine and it is represented in Fig. 13. It is assumed that the turbine has a pressure limiting mechanism, either bypass or as a relief valve in the turbine duct.

The dimensionless power, Π, finally allows the calculation of the PTO torque (turbine torque) to be reproduced by the emulator, using Eq. (58)

$$T_{PTO} = \Pi\cdot\rho_0\cdot N^2\cdot D^5 \tag{58}$$

6.2. OWC WEC emulation

The first step to implement the mathematical model of the OWC WEC in the lab is programming their equations into one of the dual-core MCUs. The results obtained from simulation and from the MCU implementation are identical, which can be observed from Figs. 14–17. In all

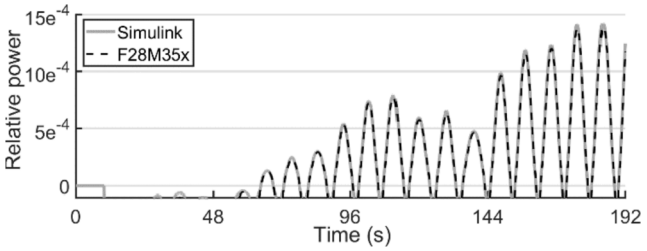

Fig. 17. Dimensionless power, **Π**.

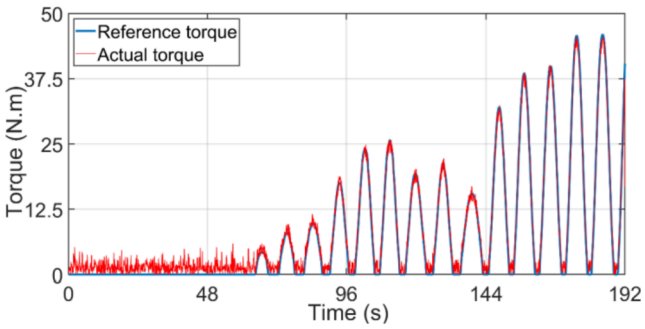

Fig. 18. Reference torque and actual torque.

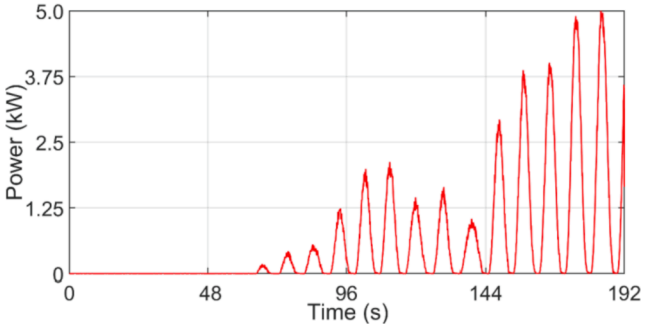

Fig. 19. PTO power.

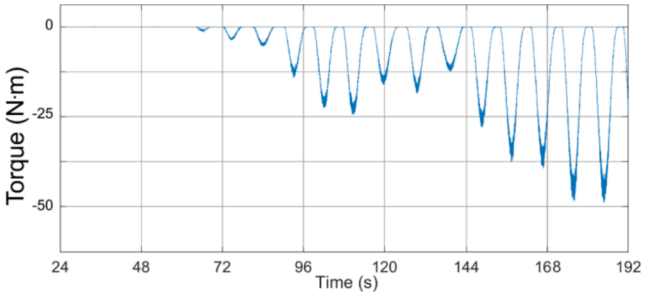

Fig. 20. Electric generator load torque.

of the three cases, the rotor speed is assumed to be constant and equal to 750 rpm, for simplification. The wave was calculated using a significant height Hs = 1.5 m and a peak period Tp = 13.78 s. The Thevenin equivalent voltage source (equivalent excitation force) is precalculated from Fig. 12 [35,36] and represented by 9600 samples of 64 bit and a sampling time of 0.02 s stored in the Flash memory of the MCU.

The following steps are carried out by the MCU in every program cycle (k):

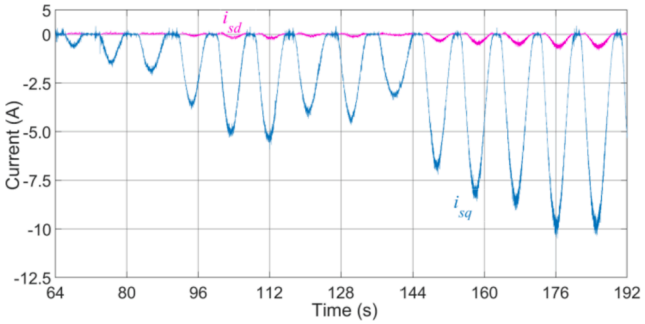

Fig. 21. Components i_{sq} and i_{sd} of the stator current.

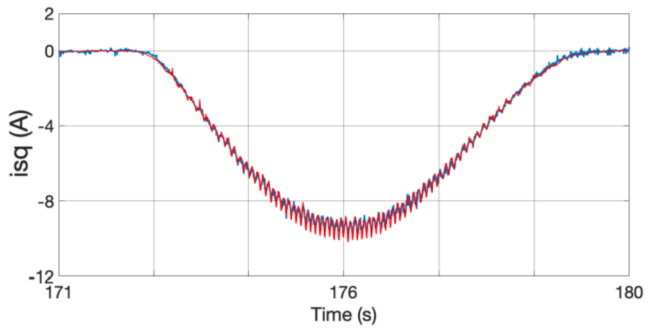

Fig. 22. Detailed view of the i_{sq} reference (red) tracking.

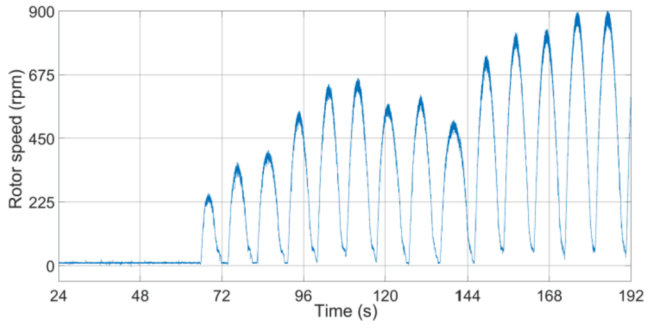

Fig. 23. Rotor speed ($N = \omega_r$).

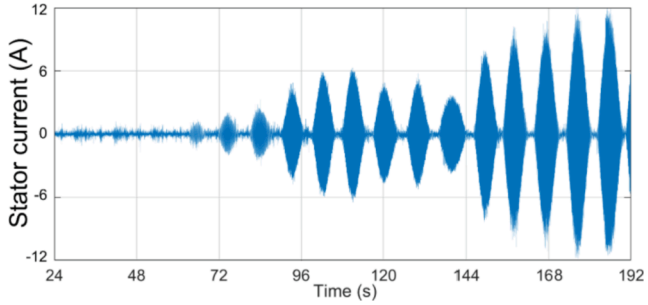

Fig. 24. PMSG stator current.

1. The (k) value of the equivalent force added to $\widehat{F}_{PTO}(k)$, Fig. 14, expressed as voltage source is used as input to the transfer function of the Thevenin circuit.

2. The transfer function obtained from the Thevenin equivalent circuit [35,36], expressed in the z-domain, speedily provides the relative velocity, $u_r(k)$, between the free surface of the water column and the body 1, Fig. 15.

3. The pressure in the air chamber, Fig. 16, is calculated using the transfer function $\frac{p(s)}{u_r(s)} = \frac{1}{\varepsilon} \cdot \frac{1}{s+\frac{1}{\varepsilon \cdot \Gamma}}$ Note that Γ depends on the rotation speed of the Wells turbine, N.

4. PTO force, $F_{PTO}(k+1) = p_{at} \cdot S_2 \cdot p(k)^*$, is used in the next cycle in step 1.

5. The dimensionless pressure in the chamber is calculated, $(k) = \frac{p(k)}{\rho_0 \cdot N(k)^2 \cdot D^2}$, where N is an input.

6. The dimensionless power of the Wells turbine, Π, is obtained by interpolation in the Π-Ψ curve, stored as a 100-values length array in Flash memory in the MCU, Fig. 17.

Notice that the relative power in Fig. 17 is repeatedly negative because in the curve of the Wells turbine, Fig. 13, low values of relative pressure imply negative relative power. However, in the emulator, the power is generated using a DC motor that can't work absorbing power since the power converter that drives it is not able to drain it to the grid. Consequently, during the experiments, the power generated by the DC motor is set to be $P \geq 0$.

7. Finally, the PTO torque, to be reproduced by the DC motor, is calculated using the dimensionless power, Π, the turbine speed, $N = \omega_r$, and the turbine physical dimensions $T_{PTO}(k) = \Pi(k) \cdot \rho_0 \cdot N(k)^2 \cdot D^5$.

The total calculation time was 583μs, although it should be noted that it was necessary to use a 64-bit *long double* data type (on a 32-bit CPU) to maintain the same degree of accuracy as in the simulation environment i.e. Simulink.

6.3. Reproduction of PTO torque and power

Using the results of the PTO torque as reference for the DC motor, a

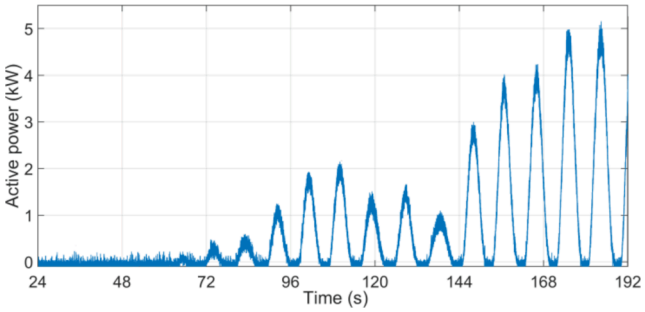

Fig. 26. Electric power delivered to the grid.

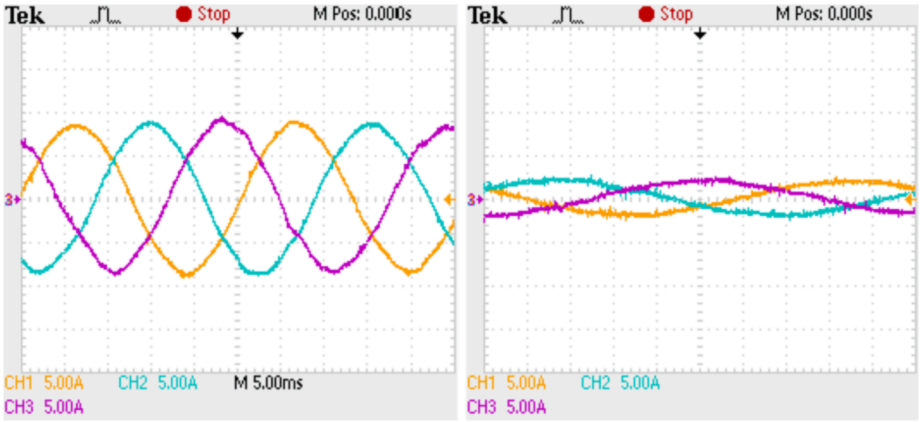

Fig. 25. PMSG stator current in three different moments of the test.

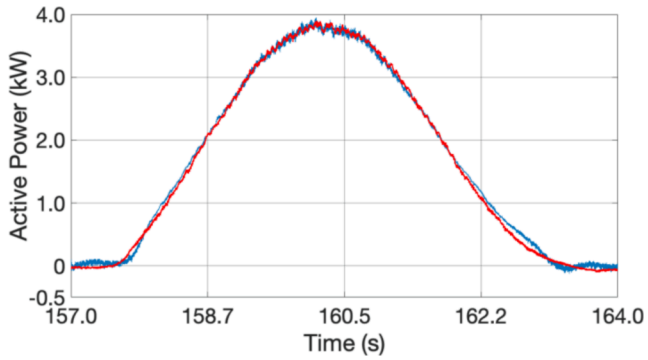

Fig. 27. Detailed view of the electric power delivered to the grid. In red, the power reference.

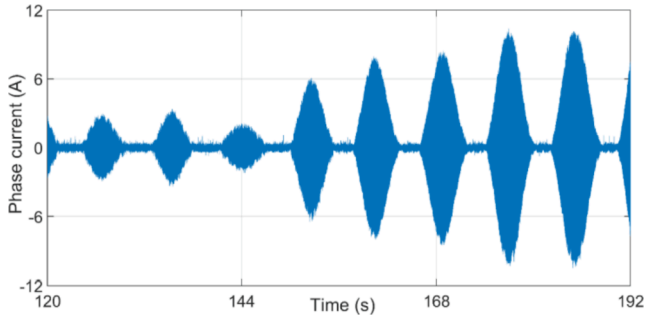

Fig. 28. Phase current generated by the grid side converter.

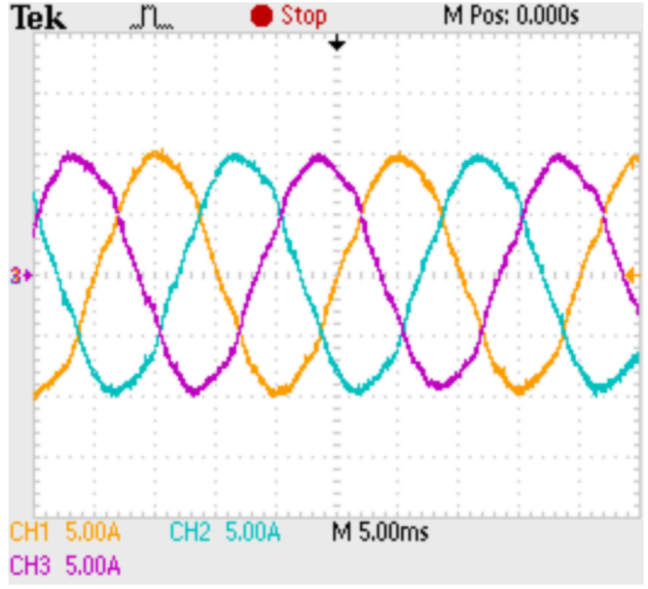

Fig. 29. Phase current generated by the grid side converter.

scale torque is generated by controlling the armature current through a hysteresis band and is based on the relationship

$$T_{DCmotor}(k) = K_T \cdot I_{DC}(k) = T_{PTO}(k) \tag{59}$$

The results are shown in Fig. 18, where a smooth blue line is the reference and the red line is the actual torque generated by the DC motor. Note that, although the hysteresis band leads to ripple in the current and torque, it allows the tracking of fast torque reference changes.

The mechanical power sent by the PTO to the electric generator is approximated by the electric power absorbed by the DC motor, Fig. 19.

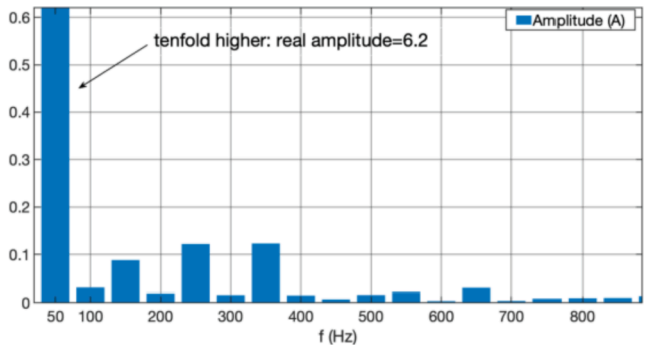

Fig. 30. Harmonic spectrum of one of the grid currents for the proposed MPPC.

6.4. Electric generator

The generator torque is controlled by the i_{sq} component of the stator current, Fig. 20, whereas the component i_{sd} controls the generator magnetic field. Both components of the current are shown in Fig. 21 and Fig. 22 shows the good reference tracking achieved by the MMPC in the MSC.

The difference between the DC motor torque and the generator load torque produces the rotor speed changes as shown in Fig. 23. The MMPC used to control the generator torque achieves an accurate tracking of the reference, obtained as the square of the rotor speed, Fig. 23.

The following figures show the PMSG stator current that generates the electric power sent to the DC-link. Fig. 24 shows the current throughout the entire test. Note the large oscillations in amplitude.

Fig. 25 shows two different moments of the test which illustrate the wide variation in amplitude and frequency featured by the stator current. The high quality of the sinusoidal waveforms can be readily observed.

6.5. Grid connection

The purpose of the grid connection is to keep the DC-link voltage constant. Hence, the power delivered to the grid must be equal to the power generated by the PMSG power. The MMPC programmed in the corresponding dual-core MCU controls the active power through the i_{sd} component of the grid current whereas $i_{sq}$is kept to zero to keep the reactive power zero. The result for the complete test is shown in Fig. 26, and Fig. 27 where the good power reference tracking achieved by the MMPC in grid connection can be observed.

The electric power sent to the grid is a consequence of the line currents generated by the grid side electronic converter. This current is highly variable, as illustrated in Fig. 28. Note that in Fig. 28 the variation of amplitude is caused, in the end, by the sea waves.

Finally, Fig. 29 shows the sinusoidal waveform of the grid current. Unlike in the case of the PMSG, now at least the frequency is constant although the amplitude is highly variable.

In laboratory conditions, the phase current shows a large first harmonic and low higher-order harmonics (1st: 6.2, 2nd: 0.03055, 3rd: 0.08815, 4th: 0.0195, 5th: 0.122, etc.), resulting in THD = 3.2%, Fig. 30. It must be taken into account that, in the laboratory, the grid is provided by an autotransformer whose voltage waveform is not perfectly sinusoidal, the filter inductances are not equal in the three phases, the inductances are not completely linear, etc.

Fig. 31 shows a basic FFT analysis performed using a Rohde & Schwarz RTA4000 oscilloscope corresponding to one of the phase currents. As expected, the harmonics gather around the SVM carrier frequency (5 kHz) and its multiples. The reason is that, unlike other MPC strategies, the proposed MMPC features constant switching frequency.

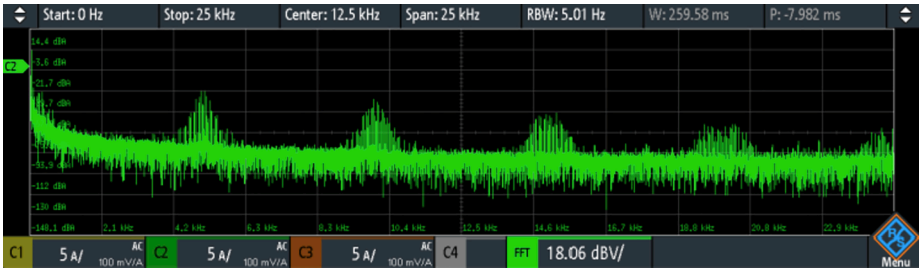

Fig. 31. FFT of one of the phase currents.

Notice that the firmware of the oscilloscope provides a relative value (dBV) with respect to an internal reference of 1Veff (dBA and 1Aeff when current clamps are used).

7. Conclusions

This paper presents a PTO control that comprises two MMPCs, one for the MSC and another for the GSC. Although the turbine torque of OWC WECs features fast and wide variations, the cost function minimization in the MMPC of the MSC achieves excellent torque reference tracking, which maximizes power generation. The GSC takes care of delivering the highly variable incoming power to the grid. The cost function minimization of the MMPC in this converter has been shown to achieve good reference tracking (in this case for the active and reactive powers). In addition, the low ripple in currents achieved by the MMPCs in the MSC and in the GSC provides high quality power to the PMSG and the grid. Furthermore, the proposed PTO control features constant switching frequency and low computational time in the modulation stage compared to other state-of-the-art MPCs.

A new model of a floating OWC WEC where the differential velocity is easily obtained by the subtraction of two electric currents in an equivalent Thevenin circuit has been presented. The use of an electric equivalence circuit results in a fast calculation of the relative velocity in an MCU, wherein it is necessary to obtain the pressure in the chamber and the PTO force. Finally, the differential velocity is used to obtain the torque generated by the PTO in an emulator in the laboratory.

The performance of the proposed dual MMPC has been demonstrated through simulations and experimental tests in the laboratory.

CRediT authorship contribution statement

Marcos Blanco: Conceptualization, Formal analysis, Investigation, Validation, Writing - review & editing. **Dionisio Ramirez:** Conceptualization, Formal analysis, Investigation, Validation, Writing - review & editing. **Mohammad Ebrahim Zarei:** Formal analysis, Investigation, Writing - original draft, Writing - review & editing, Resources. **Mahima Gupta:** Investigation, Writing - original draft, Writing - review & editing.

Declaration of Competing Interest

The authors declare that they have no known competing financial interests or personal relationships that could have appeared to influence the work reported in this paper.

Acknowledgments

The authors want to express their gratitude to D. Miguel Vicente, a researcher in WavEC – Offshore Renewable and Misael Tinoco, Master student at the UPM.

This work was partially supported by the project number DPI2017-88505-C2-1-R of I + D + i projects of “Programa Estatal de Investigacion, Desarrollo e Innovacion Orientada a los Retos de la Sociedad” of Spain.

References

[1] Falcão AFdO. Wave energy utilization: A review of the technologies. Renew Sustain Energy Rev, vol. 14, no. 3. 2010, doi: 10.1016/j.rser.2009.11.003.
[2] Davide M. Ocean Energy: Technology Market Report. Luxembourg 2019. https://doi.org/10.2760/019719.
[3] Casadei D, Profumo F, Serra G, Tani A. FOC and DTC: two viable schemes for induction motors torque control. IEEE Trans Power Electron Sep. 2002;17(5):779–87. https://doi.org/10.1109/TPEL.2002.802183.
[4] Inoue Y, Morimoto S, Sanada M. Comparative study of PMSM drive systems based on current control and direct torque control in flux-weakening control region. IEEE Trans Ind Appl Nov. 2012;48(6):2382–9. https://doi.org/10.1109/TIA.2012.2227134.
[5] Buja GS, Kazmierkowski MP. Direct torque control of PWM inverter-fed AC motors—a survey. IEEE Trans Ind Electron Aug. 2004;51(4):744–57. https://doi.org/10.1109/TIE.2004.831717.
[6] Mishra SK, Purwar S, Kishor N. Event-triggered nonlinear control of OWC ocean wave energy plant. IEEE Trans Sustain Energy Oct. 2018;9(4):1750–60. https://doi.org/10.1109/TSTE.2018.2811642.
[7] Lekube J, Garrido AJ, Garrido I. Rotational speed optimization in oscillating water column wave power plants based on maximum power point tracking. IEEE Trans Autom Sci Eng Apr. 2017;14(2):681–91. https://doi.org/10.1109/TASE.2016.2596579.
[8] M’zoughi F, Bouallegue S, Garrido AJ, Garrido I, Ayadi M. Stalling-free control strategies for oscillating-water-column-based wave power generation plants. IEEE Trans Energy Convers, vol. 33, no. 1, pp. 209–222, Mar. 2018, doi: 10.1109/TEC.2017.2737657.
[9] Lafoz M, Blanco M, Beloqui L, Navarro G, Moreno-Torres P. Dimensioning methodology for energy storage devices and wave energy converters supplying isolated loads. IET Renew Power Gener Nov. 2016;10(10):1468–76. https://doi.org/10.1049/iet-rpg.2016.0074.
[10] Villalba I, Blanco M, Pérez-Díaz JI, Fernández D, Díaz F, Lafoz M. Wave farms grid code compliance in isolated small power systems. IET Renew Power Gener Jan. 2019;13(1):171–9. https://doi.org/10.1049/iet-rpg.2018.5351.
[11] Sun T, Nielsen S. Semi-active feedforward control of a floating OWC point absorber for optimal power take-off. IEEE Trans Sustain Energy, pp. 1–1, 2019, doi: 10.1109/TSTE.2019.2923279.
[12] D. E.-I. J. of A. Mathematics and undefined 1978, “The oscillating water column wave-energy device,” academic.oup.com, Accessed: Nov. 11, 2019. [Online]. Available: https://academic.oup.com/imamat/article-abstract/22/4/423/662368.
[13] Falnes J, Perlin M. Ocean waves and oscillating systems: linear interactions including wave-energy extraction. Appl Mech Rev, vol. 56, no. 1, pp. B3–B3, Jan. 2003, doi: 10.1115/1.1523355.
[14] D. E.-J. of F. Mechanics and undefined 1982, “Wave-power absorption by systems of oscillating surface pressure distributions,” cambridge.org, Accessed: Nov. 11, 2019. [Online]. Available: https://www.cambridge.org/core/journals/journal-of-

fluid-mechanics/article/wavepower-absorption-by-systems-of-oscillating-surface-pressure-distributions/87692E82326B692716FE15F4255E4592.
[15] Bailey H, Robertson BRD, Buckham BJ. Wave-to-wire simulation of a floating oscillating water column wave energy converter. Ocean Eng Oct. 2016;125:248–60. https://doi.org/10.1016/J.OCEANENG.2016.08.017.
[16] Henriques JCC, Gato LMC, Falcão AFO, Robles E, Faÿ F-X. Latching control of a floating oscillating-water-column wave energy converter. Renew Energy May 2016;90:229–41. https://doi.org/10.1016/j.renene.2015.12.065.
[17] Henriques JCCC, Portillo JCCCC, Gato LMCMC, Gomes RPFPF, Ferreira DNN, Falcão AFOFO. Design of oscillating-water-column wave energy converters with an application to self-powered sensor buoys. Energy, vol. 112, pp. 852–867, Oct. 2016, Accessed: Nov. 11, 2019. [Online]. Available: https://www.sciencedirect.com/science/article/pii/S0360544216308283.
[18] Justino PAP, Falcão AF de O. Rotational Speed Control of an OWC Wave Power Plant, vol. 121, no. 2. American Society of Mechanical Engineers Digital Collection, 1999, pp. 65–70.
[19] Amundarain M, Alberdi M, Garrido AJ, Garrido I. Control strategies for OWC wave power plants. In: Proceedings of the 2010 American Control Conference, Jun. 2010, pp. 4319–4324, doi: 10.1109/ACC.2010.5530825.
[20] Paparella F, Monk K, Winands V, Lopes MFP, Conley D, Ringwood JV. Up-wave and autoregressive methods for short-term wave forecasting for an oscillating water column. IEEE Trans Sustain Energy, vol. 6, no. 1, 2015, doi: 10.1109/TSTE.2014.2360751.
[21] Fusco F, Ringwood JV. Short-term wave forecasting for real-time control of wave energy converters. IEEE Trans Sustain Energy, vol. 1, no. 2, 2010, doi: 10.1109/TSTE.2010.2047414.
[22] Hatalis K, Pradhan P, Kishore S, Blum RS, Lamadrid AJ. Multi-step forecasting of wave power using a nonlinear recurrent neural network. In: IEEE Power and Energy Society General Meeting, 2014, vol. 2014-October, no. October, doi: 10.1109/PESGM.2014.6939370.
[23] Schoen MP, Hals J, Moan T. Wave prediction and fuzzy logic control of wave energy converters in irregular waves. In: 2008 Mediterranean Conference on Control and Automation - Conference Proceedings, MED'08; 2008. https://doi.org/10.1109/MED.2008.4602036.
[24] Dekka A, Wu B, Yaramasu V, Fuentes RL, Zargari NR. Model predictive control of high-power modular multilevel converters—an overview. IEEE J Emerg Sel Top Power Electron Mar. 2019;7(1):168–83. https://doi.org/10.1109/JESTPE.2018.2880137.
[25] Zarei ME, Nicolas CV, Arribas JR, Ramirez D. Four-switch three-phase operation of grid-side converter of doubly fed induction generator with three vectors predictive direct power control strategy. IEEE Trans Ind Electron Oct. 2019;66(10):7741–52. https://doi.org/10.1109/TIE.2018.2880672.
[26] Rodriguez J, et al. State of the art of finite control set model predictive control in power electronics. IEEE Trans Ind Informatics May 2013;9(2):1003–16. https://doi.org/10.1109/TII.2012.2221469.
[27] Zarei ME, Gupta M, Ramirez D, Martinez-Rodrigo F. Switch fault tolerant model-based predictive control (MPC) of a VSC connected to the grid. IEEE J Emerg Sel Top Power Electron 2019. https://doi.org/10.1109/JESTPE.2019.2956042.
[28] Ramirez D, Mendonça H, Blanco M, Martinez F. Non-linear vector current source for the control of permanent magnet synchronous generators in wave energy applications. IET Renew Power Gener Oct. 2019;13(13):2409–17. https://doi.org/10.1049/iet-rpg.2019.0122.
[29] Ramirez D, Blanco M, Zarei ME, Gupta M. Robust control of a floating OWC WEC under open-switch fault condition in one or in both VSCs. IET Renew Power Gener Jul. 2020. https://doi.org/10.1049/iet-rpg.2020.0203.
[30] Henriques JCC, Portillo JCC, Gato LMC, Gomes RPF, Ferreira DN, Falcão AFO. Design of oscillating-water-column wave energy converters with an application to self-powered sensor buoys. Energy Oct. 2016;112:852–67. https://doi.org/10.1016/j.energy.2016.06.054.
[31] Gomes RPF, Henriques JCC, Gato LMC, Falcão AFO. Wave power extraction of a heaving floating oscillating water column in a wave channel. Renew Energy Dec. 2016;99:1262–75. https://doi.org/10.1016/j.renene.2016.08.012.
[32] Henriques JCC, Lopes MFP, Gomes RPF, Gato LMC, Falcão AFO. On the annual wave energy absorption by two-body heaving WECs with latching control. Renew Energy Sep. 2012;45:31–40. https://doi.org/10.1016/j.renene.2012.01.102.
[33] Falcão AFO, Henriques JCC. Oscillating-water-column wave energy converters and air turbines: A review. Renewable Energy, vol. 85. Elsevier Ltd, pp. 1391–1424, Jan. 01, 2016, doi: 10.1016/j.renene.2015.07.086.
[34] Henriques JCC, Portillo JCC, Sheng W, Gato LMC, Falcão AFO. Dynamics and control of air turbines in oscillating-water-column wave energy converters: Analyses and case study. Renew Sustain Energy Rev Sep. 2019;112:571–89. https://doi.org/10.1016/j.rser.2019.05.010.
[35] Yu Z, Falnes J. State-space modelling of a vertical cylinder in heave. Appl Ocean Res Oct. 1995;17(5):265–75. https://doi.org/10.1016/0141-1187(96)00002-8.
[36] JohannesFalnes. STATE-SPACE MODELLING OF DYNAMIC SYSTEMS IN OCEAN ENGINEERING. 1998, Accessed: Nov. 11, 2019. [Online]. Available: https://www.semanticscholar.org/paper/STATE-SPACE-MODELLING-OF-DYNAMIC-SYSTEMS-IN-OCEAN-JohannesFalnes/9981dfa8e16caf706680e4d9df7fa7f6f69482a0.